

Electrically controlled emission from singlet and triplet exciton species in atomically thin light-emitting diodes

Andrew Y. Joe ¹, Luis A. Jauregui,² Kateryna Pistunova,¹ Andrés M. Mier Valdivia,³ Zhengguang Lu,^{4,5} Dominik S. Wild ¹, Giovanni Scuri ¹, Kristiaan De Greve,^{1,6,*} Ryan J. Gelly,¹ You Zhou,^{1,6,7} Jiho Sung,^{1,6} Andrey Sushko ¹, Takashi Taniguchi,⁸ Kenji Watanabe,⁹ Dmitry Smirnov,⁴ Mikhail D. Lukin,¹ Hongkun Park,^{1,6} and Philip Kim^{1,3,†}

¹*Department of Physics, Harvard University, Cambridge, Massachusetts 02138, USA*

²*Department of Physics and Astronomy, University of California, Irvine, California 92697, USA*

³*John A. Paulson School of Engineering and Applied Sciences, Harvard University, Cambridge, Massachusetts 02138, USA*

⁴*National High Magnetic Field Laboratory, Tallahassee, Florida 32310, USA*

⁵*Department of Physics, Florida State University, Tallahassee, Florida 32306, USA*

⁶*Department of Chemistry and Chemical Biology, Harvard University, Cambridge, Massachusetts 02138, USA*

⁷*Department of Materials Science and Engineering, University of Maryland, College Park, Maryland 20742, USA*

⁸*International Center for Materials Nanoarchitectonics, National Institute for Materials Science, 1-1 Namiki, Tsukuba 305-0044, Japan*

⁹*Research Center for Functional Materials, National Institute for Materials Science, 1-1 Namiki, Tsukuba 305-0044, Japan*



(Received 13 December 2020; revised 7 April 2021; accepted 12 April 2021; published 29 April 2021)

We report electrically tunable spin singlet and triplet exciton emission from atomically aligned transition metal dichalcogenide (TMD) heterostructures. The observation of these states in both 0° and 60° heterostructures provides the stacking orientation degree of freedom for polarization switching in interlayer excitons. We confirm the spin configurations of the light-emitting excitons employing magnetic fields to measure effective exciton g factors. The interlayer tunneling current across the TMD heterostructure enables the electrical generation of singlet and triplet exciton emission in this atomically thin p-n junction. We demonstrate tunability between the singlet and triplet exciton photoluminescence via electrostatic gates and excitation power. By tuning the gates and interlayer bias voltage, the electroluminescence of the singlet and triplet can be switched with ratios of 10:1. Atomically thin TMD heterostructure light-emitting diodes thus enable a route for optoelectronic devices that can configure spin and valley quantum states independently.

DOI: [10.1103/PhysRevB.103.L161411](https://doi.org/10.1103/PhysRevB.103.L161411)

Semiconducting transition metal dichalcogenides (TMDs) exhibit extraordinary excitonic effects when reduced to the two-dimensional limit [1–3]. Monolayer TMDs have large exciton binding energies [4] and spin-valley locking [5,6], which can be harnessed for optoelectronic [7,8] and valleytronic [6] applications. When certain monolayer TMDs are stacked together to form heterobilayers such as WSe₂/MoSe₂ [9–17], MoSe₂/MoS₂ [18], or WS₂/MoS₂ [19–21], energetically favorable interlayer excitons (IEs) can form across the atomically sharp interfaces owing to their type-II band alignment [22] and ultrafast charge transfer [18–20] between the layers. The resulting IEs have long lifetimes [9,14,15], a permanent out-of-plane dipole moment [10,14], and modified optical selection rules [10,11,13,23,24] due to the electrons and holes residing in separate layers. When the heterostructures are electron or hole doped, the IEs bind with free carriers to form charged interlayer excitons (CIEs) [14]. Furthermore, the IEs are predicted to have modified selection rules allowing emission from both singlet (electron and hole with opposite

spin) and triplet (electron and hole with the same spin) excitons with opposite polarization properties [23–25], which provides a material platform with two long-lived, electrically tunable IE states.

The singlet and triplet interlayer exciton states, with opposite spin characteristics, could be used as the basis for polarization switches [10] in excitonic quantum devices. However, since the optical selection rules differ for different atomic registries of the TMD heterostructure, the IE emission spectra, even qualitatively, vary between studies without consistent observation of both singlet and triplet states or specifications of the heterostructure stacking configuration [10,11,13,26,27]. Theoretical studies have predicted selection rules for TMD heterostructures based on the stacking orientation, either 0° aligned or 60° aligned, and atomic registry, which provide a quasiangular momentum to brighten singlet and triplet optical transitions [23–25]. While singlet and triplet interlayer excitons have been observed in 60° aligned heterostructures [26–28], the observation of these states in 0° aligned heterostructures have remained elusive. The 0° aligned heterostructures are predicted to have flipped polarization coupling to the lower and upper transitions, giving an additional degree of freedom for valleytronic devices. Further complications arise from the presence of spatially periodic moiré potentials in small twist angle structures [29–36]. While

*Present address: IMEC, 3001 Leuven, Belgium.

†Author to whom correspondence should be addressed: pkim@physics.harvard.edu

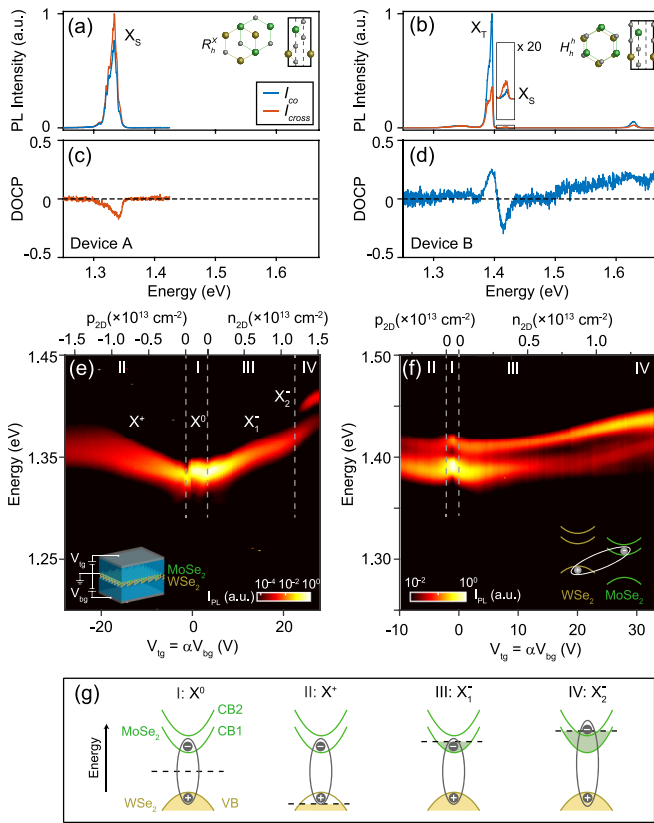


FIG. 1. Photoluminescence of interlayer excitons in MoSe₂/WSe₂ heterostructures. (a),(b) Polarization resolved photoluminescence (PL) from devices A and B, respectively. Excitation power, $P = 0.5 \mu\text{W}$ and $100 \mu\text{W}$, respectively, is used to compare all existing exciton species. Inset: Lowest energy stacking configuration for 0° and 60° heterostructures. (c),(d) Degree of circular polarization (DOCP) extracted from (a) and (b). (e),(f) PL vs $V_{\text{ig}} = \alpha V_{\text{bg}}$, where α is based on the h -BN thicknesses, for devices A and B, respectively. Left inset: device schematic and direction of applied gate voltages. Right inset: band schematic of an interlayer exciton between the conduction band of MoSe₂ and valence band of WSe₂. (g) Reduced band diagrams of the MoSe₂/WSe₂ heterostructure showing the upper (CB2) and lower (CB1) conduction bands of MoSe₂ and the valence band of WSe₂ (VB). The exciton and Fermi energy (black dashed line) is drawn for each regime marked in (e) and (f). The green (MoSe₂) and yellow (WSe₂) shaded areas indicate filled electron bands.

a multitude of sharp, quantum emitterlike peaks from moiré-trapped interlayer excitons emerge at very low excitation power, their selection rules follow that of the broader, free interlayer excitons, which dominate at higher powers [37–41]. In this work, we demonstrate electrostatic doping and interlayer bias-controlled spin singlet and triplet free interlayer exciton emission in 0° and 60° MoSe₂/WSe₂ heterostructures.

Our experiments employ h -BN encapsulated WSe₂/MoSe₂ devices with top and bottom gates, and electrically transparent contacts [Fig. 1(e), left inset], as described in our previous work [14]. We use a dual-gating scheme where the top-gate voltage (V_{tg}) and the back-gate voltage (V_{bg}) have the same polarity, achieving higher carrier densities than in

previous IE studies [10,14,15] (see details in Supplemental Material Sec. 1 [42]). Furthermore, separate electrical contacts made for MoSe₂ and WSe₂ layers allow operating the device as an atomically thin p-n diode where the current can flow across the heterostructure interface. Below we focus on two representative devices with 0° (device A) and 60° (device B) stacking orientations.

Figures 1(a) and 1(b) show a comparison of the photoluminescence (PL) spectrum for device A and B at neutral doping with circularly co- and cross-polarized exciton emission (I_{co} and I_{cross} , respectively). In device A, we observe only a single peak at ~ 1.34 eV. For device B, there are two peaks, one at ~ 1.39 eV and the other at ~ 1.41 eV, with a separation of ~ 25 meV. As shown in Figs. 1(c) and 1(d), the degree of circular polarization (DOCP), computed from $\frac{I_{\text{co}} - I_{\text{cross}}}{I_{\text{co}} + I_{\text{cross}}}$, of the lower energy peak at 1.39 eV in device B is positive, suggesting that the chirality of the light emitted remains unchanged, unlike the higher energy peak in device B and the peak in device A. The observation of two peaks with opposite DOCP in device B is consistent with previous experimental results for 60° aligned heterostructures [26,27] and their selection rules [24,25]. Thus, we tentatively identify the lower and higher energy peaks as triplet (X_T) and singlet excitons (X_S), respectively, while the emission energy and DOCP for device A are consistent with a 0° heterostructure [11].

The PL spectrum can further be modified by applying gate voltages on the devices. Figures 1(e) and 1(f) show the PL spectrum from devices A and B as a function of $V_{\text{ig}} = \alpha V_{\text{bg}}$, where $\alpha = 0.617$ or 1.4 for the two devices (based on each device's h -BN thicknesses), respectively. In this gate voltage configuration, we can maximize our achievable two-dimensional (2D) carrier density $n_{2\text{D}}$. We identify four distinct gate regions, marked by I–IV, from the electrostatic doping of the heterostructure [Fig. 1(g)]. We verify the doping of the layers by measuring the intralayer exciton absorption spectra as a function of the gate voltage (see Supplemental Material Fig. 3 [42]).

The gate dependent PL shows strong atomic stacking registry dependence. For device A [Fig. 1(e)], only neutral interlayer excitons labeled as X^0 appear in region I. In region II (III), the Fermi energy crosses the valence band of WSe₂ [lower conduction band (CB1) of MoSe₂] and we begin to p dope (n dope) the heterostructure forming CIEs, X^+ (X_1^-). The discontinuities in the PL energy between regions I/II and I/III are attributed to CIE binding energies of ~ 15 meV and ~ 10 meV, respectively [14]. In region IV, when the electron density is further increased, an additional PL peak, X_2^- , appears ~ 25 meV above the X_1^- peak, which overtakes in intensity with increasing $n_{2\text{D}}$. This additional exciton feature is likely related to reaching the upper conduction band of MoSe₂ (CB2). For device B [Fig. 1(f)], we observe a similar discontinuity in emission energy when entering regions II and III due to CIE formation but find the higher energy peak to always be present as we tune the carrier density.

To understand the angular momentum characteristics of the interlayer excitons, we measure PL under magnetic fields to determine the effective Zeeman splitting of the exciton species. We perform polarization-resolved PL measurements as a function of magnetic field (B) using a cross-polarized measurement scheme [see Supplemental Material Fig. 4(a)

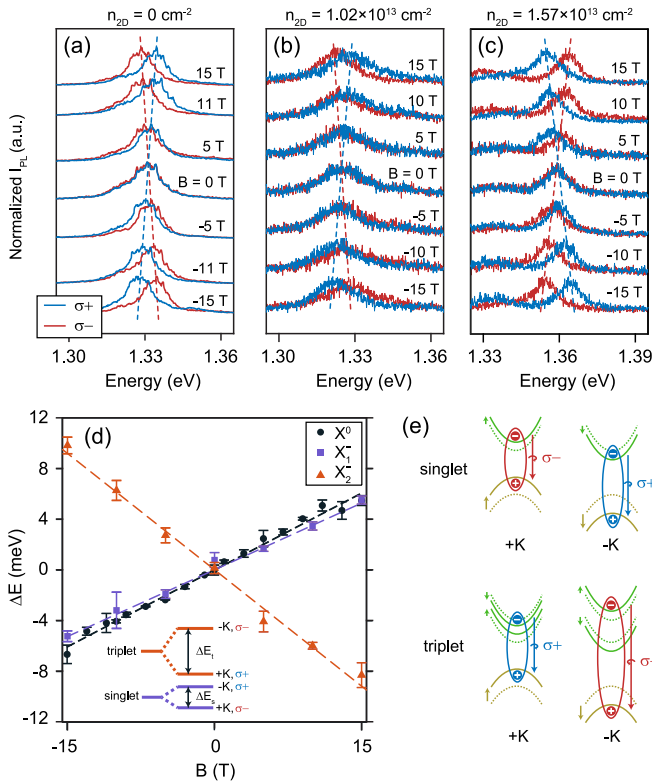


FIG. 2. Experimental evidence of spin-singlet and spin-triplet excitons via magnetic field in device A. (a)–(c) Polarization-resolved photoluminescence (PL) spectra at $n_{2D} = 0$, $1.02 \times 10^{13} \text{ cm}^{-2}$, and $1.57 \times 10^{13} \text{ cm}^{-2}$, respectively, for characteristic magnetic fields (B) using a cross-polarized measurement scheme (see Supplemental Material Sec. 4 [42]). Blue (red) curves are $\sigma+$ ($\sigma-$) collection. The dashed lines serve as a guide to the eye. (d) PL energy splitting ($\Delta E = E_{\sigma+} - E_{\sigma-}$) as a function magnetic field for X^0 , X_1^- , and X_2^- . Error bars are calculated from the fitting of the peak position. The dashed lines are linear fits to the energy splitting giving $g_0 = 6.99 \pm 0.35$, $g_1 = 6.06 \pm 0.58$, and $g_2 = -10.6 \pm 1.0$. Inset: Zeeman splitting for the singlet and triplet excitons in the exciton particle picture and the circular polarization light coupling. (e) Band diagrams and Zeeman splitting for the singlet and triplet transitions without (dashed lines) and with (solid lines) magnetic field.

[42]]. Figures 2(a)–2(c) show the normalized $\sigma+$ (blue) and $\sigma-$ (red) PL spectra measured in device A at $n_{2D} = 0$, $1.02 \times 10^{13} \text{ cm}^{-2}$ and $1.57 \times 10^{13} \text{ cm}^{-2}$, respectively. From these polarization-resolved spectra, we obtain the PL energy splitting between the circularly polarized light ($\Delta E = E_{\sigma+} - E_{\sigma-}$) as a function of B . Figure 2(d) shows that the measured energy difference follows a linear relation $\Delta E = g\mu_B B$, where g is the effective g factor and μ_B is the Bohr magneton. From the slope of the measured relation between ΔE and B , we obtain the effective g factors for X^0 , X_1^- , and X_2^- : $g_0 = 6.99 \pm 0.35$, $g_1 = 6.06 \pm 0.58$, and $g_2 = -10.6 \pm 1.0$, respectively. Interestingly, the g factor for X_2^- is greater than and has the opposite sign of g_0 and g_1 , implying X_2^- has an additional Zeeman splitting contribution and that the chiral light coupling to the K valleys is flipped compared to X^0 or X_1^- . The observation of a higher energy emission in region IV also suggests that transitions between the highest WSe_2 K -valley

valence band and both spin-split MoSe_2 K -valley conduction bands are allowed. This would indicate that the higher energy peak is an emissive triplet transition with an in-plane dipole moment, unlike dark triplet excitons in monolayers [43–45].

The experimental observations of $\sim 25 \text{ meV}$ splitting between X_2^- and X_1^- as well as the opposite polarization characteristics are consistent with spin-singlet and -triplet transition selection rules in the 0° aligned heterostructure (see Supplemental Material Sec. 5 [42]). Quantitative evidence for the singlet and triplet states and opposite circular polarization coupling is revealed by calculating the expected exciton g factors using a single electron band picture [9,46]. The expected g factor is based on the Zeeman shift of each electron band [Fig. 2(e)] without considering any additional excitonic effects under magnetic field (see further details in Supplemental Material Sec. 6 [42]). More detailed theoretical studies show that our simplified model uses reasonable assumptions [25,46,47]. From this model, we calculate the singlet and triplet g factors to be $g_{\text{singlet}}^{0\text{-theory}} \approx 7.1$ and $g_{\text{triplet}}^{0\text{-theory}} \approx -11.1$, respectively. These calculated g factors are in excellent agreement with experimentally observed values both in terms of sign and magnitude. Thus, we confirm X_1^- and X_2^- as singlet and triplet excitonic transitions, respectively. We note that unlike the traditional picture of singlet and triplet states, the degeneracy of interlayer exciton singlet and triplet states is already broken due to spin-orbit coupling. These states split differently under magnetic field as shown in the inset of Fig. 2(d) in the exciton particle picture. Similarly, we performed magneto-PL measurement in a separate 60° aligned sample and confirmed the selection rules and associated large triplet transition g factor, $g_{\text{triplet}}^{60\text{-stack}} \approx -15.1 \pm 0.4$ (see Supplemental Material Sec. 7 [42]) in agreement with theory and previous measurements [27]. Thus, we confirm the emission of triplet excitons in 0° heterostructures occur, but only at high n_{2D} .

From this analysis, we can now assign the peaks in the PL spectra as either singlet or triplet states. In regions I–III, X^0 , X^+ , and X_1^- all have transitions from CB1, allowing us to assign them as singlet neutral or singlet charged excitons. In region IV, the X_2^- peak is a transition from CB2 in the presence of free carriers and is therefore a triplet charged exciton. Energetically, the triplet charged exciton can form with an electron in CB1 of either K valley in MoSe_2 , but further studies are required for a more detailed understanding. The emergence of X_2^- only after sufficient band filling can be explained by the relative dipole strengths of the singlet and triplet excitons. The lifetimes of X_1^- and X_2^- at high n_{2D} were measured to be $\tau_1 = 6.08 \pm 0.01 \text{ ns}$ and $\tau_2 = 6.12 \pm 0.02 \text{ ns}$ (see Supplemental Material Fig. 8, inset [42]), respectively, suggesting the optical dipole strength of the two exciton species is similar (see Supplemental Material Sec. 8 [42]), consistent with theoretical calculations [24,25].

We find that the relative intensity of singlet and triplet exciton emission can be tuned by electrostatic doping and power of the laser excitation. Figures 3(a) and 3(b) show the power dependence of the normalized PL emission in devices A and B. The double peaked features near 1.34 and 1.37 eV in devices A and B, respectively, are attributed to CIEs due to changes in residual doping by the excitation power. We

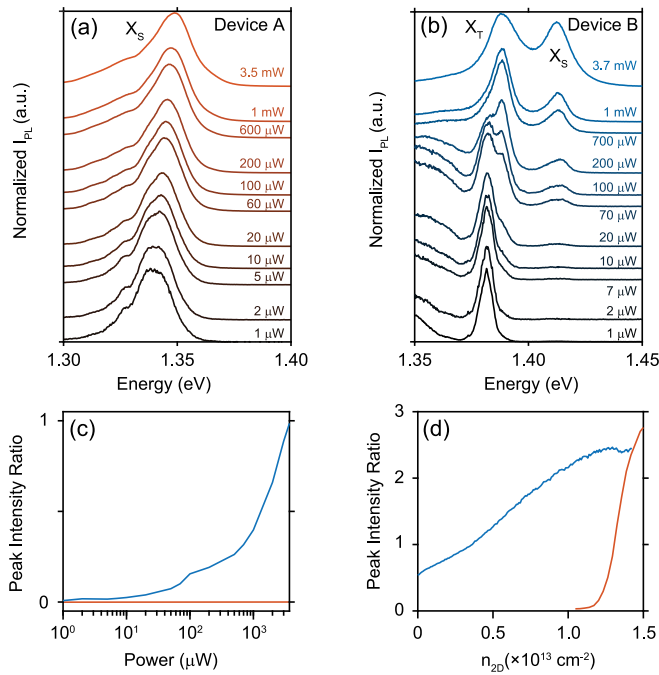


FIG. 3. Tunable interlayer exciton species via excitation power and carrier density. (a),(b) Power (P) dependence of the normalized photoluminescence (PL) spectra at $V_{\text{tg}} = \alpha V_{\text{bg}} = 0$ V for devices A and B, respectively. (c) Peak intensity ratio between the higher energy peak and the lower energy peak for device A (orange) and device B (blue) as a function of excitation power at $V_{\text{tg}} = \alpha V_{\text{bg}} = 0$ V. The higher energy peak does not appear at this carrier density in device A. (d) The same peak intensity ratio as a function of carrier density at $P = 6 \mu\text{W}$ for device A (orange) and $P = 100 \mu\text{W}$ for device B (blue).

find that device A at neutral doping is always dominated by lower energy singlet emission without triplet emission even at high excitation powers. Device B even at neutrality, on the other hand, has a higher energy singlet peak (~ 1.42 eV) which becomes more prominent at higher powers. In the strongly nonequilibrium state at the largest excitation, the singlet and triplet emission are about similar intensity [Fig. 3(c)]. While the excitation power can show a limited range of singlet/triplet emission ratio, the electrostatic doping tuned by the gate can vary the triplet/singlet emission ratio in a wide range. Figure 3(d) shows that the initially dominant singlet emission in device A turned to more than 70% triplet emission in the high doping range ($n_{2D} > 1.4 \times 10^{13} \text{ cm}^{-2}$), providing a singlet and triplet device where the emission of one state can be completely turned off. In device B, the inverse ratio can be tuned, with the singlet/triplet emission ratio varying between 0.5 and 2.5 over a similar carrier density range. Thus, the $\text{MoSe}_2/\text{WSe}_2$ heterostructure provides a platform for fully tunable singlet-triplet exciton emission via electrical gates, excitation power, and the stacking registry.

Utilizing electrical contacts in WSe_2 and MoSe_2 layers, we can operate the device as a gate tunable atomically thin p-n diode [14,17,54], where the interlayer tunneling current across the heterostructure interface can generate singlet and triplet exciton emission. Figure 4(a) shows the current (I_{ds}) vs drain-source voltage (V_{ds}) curve at $V_{\text{tg}} = \alpha V_{\text{bg}} = 10$ V,

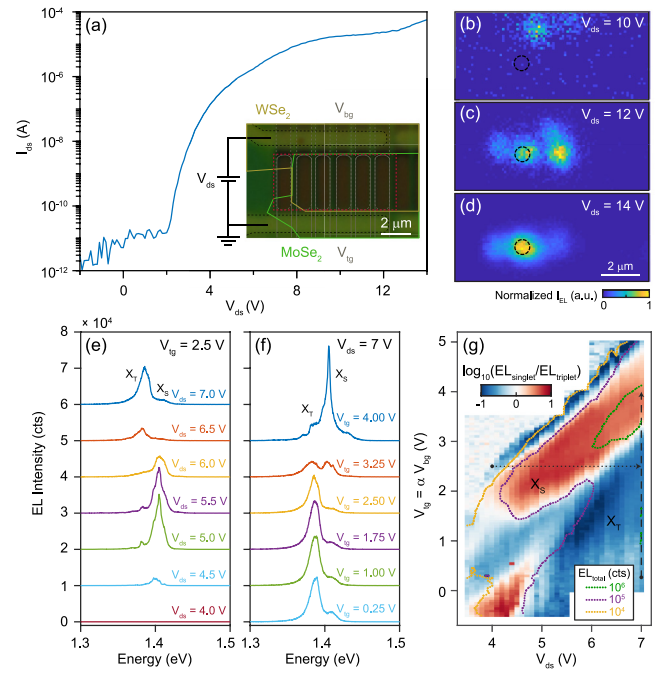


FIG. 4. Electrical generation of singlet and triplet exciton species in device B. (a) I - V characteristics of device B at $V_{\text{tg}} = \alpha V_{\text{bg}} = 10$ V, where $\alpha = 1.4$ is based on the h -BN thicknesses. Inset: Optical image of the sample with yellow (green) lines indicating WSe_2 (MoSe_2) area, gray solid (dashed) lines indicating V_{tg} (V_{bg}), black dashed lines outline the contacts, and the red dashed rectangle to indicate sample area of interest in (b)–(d). (b)–(d) Spatial maps of normalized electroluminescence (EL) generated from the sample when in forward bias ($V_{\text{ds}} = 10, 12,$ and 14 V). The black dashed circle indicates the collection spot for the spectra. (e) EL spectra as a function of V_{ds} at fixed $V_{\text{tg}} = \alpha V_{\text{bg}} = 2.5$ V. (f) EL spectra as a function of $V_{\text{tg}} = \alpha V_{\text{bg}}$ at fixed $V_{\text{ds}} = 7$ V. (g) The log of the ratio between the integrated EL emission from singlet and triplet interlayer excitons as a function of V_{ds} and $V_{\text{tg}} = \alpha V_{\text{bg}}$ showing voltage regions with singlet and triplet dominant emission. The colored dotted lines show contours of the total integrated EL. The black dotted and dashed lines correspond to the linecuts for spectra in (e) and (f), respectively.

where $\alpha = 1.4$, for device B, demonstrating rectifying diode behavior as expected for a type-II aligned heterostructure. Figures 4(b)–4(d) show the spatial distribution of the electroluminescence (EL) emission from the red outlined area of the heterostructure [Fig. 4(a) inset] under the same gate conditions at different V_{ds} in the high bias regime. We find that the spatial distribution of the emission is inhomogeneous, presumably due to disorders in the channel and the lateral gaps between the gate structures (see Supplemental Material Sec. 9 [42]). The emission position shifts sensitively with V_{ds} and V_{tg} , which tune the current distribution in the channel (see Supplemental Material Sec. 10 [42]). Figures 4(e) and 4(f) show the EL spectra collected at a fixed location of the sample [marked by dashed black circle in Figs. 4(b)–4(d)] for various gate and bias configurations [along the dotted and dashed line in Fig. 4(g), respectively]. We demonstrate complete tunability between singlet and triplet exciton EL emission as a function of V_{ds} and V_{tg} . Figure 4(g) maps out the log of the ratio between the integrated singlet and triplet emission as

a function of V_{ds} and V_{tg} , showing voltage conditions where either the singlet or triplet emission is dominant. The ratio of the EL emission between singlet and triplet, or triplet and singlet, approaches as large as 10:1. The observed switching is accompanied by enhancements in the total EL emission (see Supplemental Material Sec. 11 for details [42]), but further studies are required to fully understand the gate dependence. We have demonstrated electrical generation that can be gate-tuned to be dominated by either singlet or triplet exciton emission, demonstrating a light-emitting diode (LED) with selectable emission between opposite spin and polarizability characteristics.

Our capability of gate tuning to access the higher conduction band with opposite spin allows us to create charged excitons with singlet and triplet spin configurations and opposite chiral light coupling. The observation of the elusive triplet interlayer exciton state allows for the stacking configuration to be used in choosing the lowest energy spin state of the interlayer exciton. We demonstrate control of singlet and triplet interlayer exciton emission via electrostatic doping, optical pump power, and injection current. The observation of these states under the presence of charges means circularly polarized light coupling in singlet and triplet excitons can switch between fermionic and bosonic character, which could be utilized in novel quantum devices. Electrical generation of tunable singlet and triplet excitons in TMD heterostructures, combining long EL lifetime [14] with local gate

engineering [55], paves the way towards independently controlling chiral, valley, and spin quantum states in valleytronic devices.

We thank S. Fang for helpful discussions. We acknowledge support from the DoD Vannevar Bush Faculty Fellowship (Grant No. N00014-18-1-2877 for P.K., Grant No. N00014-16-1-2825 for H.P.), AFOSR MURI (Grant No. FA9550-17-1-0002), NSF and CUA (Grants No. PHY-1506284 and No. PHY-1125846 for H.P. and M.D.L.), ARL (Grant No. W911NF1520067 for H.P. and M.D.L.), and Samsung Electronics (for P.K. and H.P.). Z.L. and D.S. acknowledge support from the U.S. Department of Energy (Grant No. DE-FG02-07ER46451) for magnetophotoluminescence measurements performed at the National High Magnetic Field Laboratory, supported by National Science Foundation through Grants No. NSF/DMR-1157490 and No. DMR-1644779 and the State of Florida. K.W. and T.T. acknowledge support from the Elemental Strategy Initiative conducted by the MEXT, Japan, Grant No. JPMXP0112101001, JSPS KAKENHI Grant No. JP20H00354, and the CREST (Grant No. JPMJCR15F3), JST. This material is based upon work supported by the National Science Foundation Graduate Research Fellowship under Grant No. DGE1745303. Any opinion, findings, and conclusions or recommendations expressed in this material are those of the author(s) and do not necessarily reflect the views of the National Science Foundation.

-
- [1] K. F. Mak, C. Lee, J. Hone, J. Shan, and T. F. Heinz, Atomically Thin MoS_2 : A New Direct-Gap Semiconductor, *Phys. Rev. Lett.* **105**, 136805 (2010).
- [2] G. Scuri, Y. Zhou, A. A. High, D. S. Wild, C. Shu, K. De Greve, L. A. Jauregui, T. Taniguchi, K. Watanabe, P. Kim, M. D. Lukin, and H. Park, Large Excitonic Reflectivity of Monolayer MoSe_2 Encapsulated in Hexagonal Boron Nitride, *Phys. Rev. Lett.* **120**, 037402 (2018).
- [3] H. H. Fang, B. Han, C. Robert, M. A. Semina, D. Lagarde, E. Courtade, T. Taniguchi, K. Watanabe, T. Amand, B. Urbaszek, M. M. Glazov, and X. Marie, Control of the Exciton Radiative Lifetime in van Der Waals Heterostructures, *Phys. Rev. Lett.* **123**, 067401 (2019).
- [4] A. Chernikov, T. C. Berkelbach, H. M. Hill, A. Rigosi, Y. Li, O. B. Aslan, D. R. Reichman, M. S. Hybertsen, and T. F. Heinz, Exciton Binding Energy and Nonhydrogenic Rydberg Series in Monolayer WS_2 , *Phys. Rev. Lett.* **113**, 076802 (2014).
- [5] K. F. Mak, K. He, J. Shan, and T. F. Heinz, Control of valley polarization in monolayer MoS_2 by optical helicity, *Nat. Nanotechnol.* **7**, 494 (2012).
- [6] M. Onga, Y. Zhang, T. Ideue, and Y. Iwasa, Exciton hall effect in monolayer MoS_2 , *Nat. Mater.* **16**, 1193 (2017).
- [7] C. H. Lee, G. H. Lee, A. M. Van Der Zande, W. Chen, Y. Li, M. Han, X. Cui, G. Arefe, C. Nuckolls, T. F. Heinz, J. Guo, J. Hone, and P. Kim, Atomically thin p-n junctions with van der waals heterointerfaces, *Nat. Nanotechnol.* **9**, 676 (2014).
- [8] B. W. H. Baugher, H. O. H. Churchill, Y. Yang, and P. Jarillo-Herrero, Optoelectronic devices based on electrically tunable P-n diodes in a monolayer dichalcogenide, *Nat. Nanotechnol.* **9**, 262 (2014).
- [9] P. Nagler, M. V. Ballottin, A. A. Mitioglu, F. Mooshammer, N. Paradiso, C. Strunk, R. Huber, A. Chernikov, P. C. M. Christianen, C. Schüller, and T. Korn, Giant magnetic splitting inducing near-unity valley polarization in van der waals heterostructures, *Nat. Commun.* **8**, 1551 (2017).
- [10] A. Ciarrocchi, D. Unuchek, A. Avsar, K. Watanabe, T. Taniguchi, and A. Kis, Polarization switching and electrical control of interlayer excitons in two-dimensional van der waals heterostructures, *Nat. Photonics* **13**, 131 (2019).
- [11] W. T. Hsu, L. S. Lu, P. H. Wu, M. H. Lee, P. J. Chen, P. Y. Wu, Y. C. Chou, H. T. Jeng, L. J. Li, M. W. Chu, and W. H. Chang, Negative circular polarization emissions from $\text{WSe}_2/\text{MoSe}_2$ commensurate heterobilayers, *Nat. Commun.* **9**, 1356 (2018).
- [12] B. Müller, A. Steinhoff, B. Pano, J. Klein, F. Jahnke, A. Holleitner, and U. Wurstbauer, Long-Lived direct and indirect interlayer excitons in van der waals heterostructures, *Nano Lett.* **17**, 5229 (2017).
- [13] A. T. Hanbicki, H. J. Chuang, M. R. Rosenberger, C. S. Hellberg, S. V. Sivaram, K. M. McCreary, I. I. Mazin, and B. T. Jonker, Double indirect interlayer exciton in a $\text{MoSe}_2/\text{WSe}_2$ van der waals heterostructure, *ACS Nano* **12**, 4719 (2018).
- [14] L. A. Jauregui, A. Y. Joe, K. Pistunova, D. S. Wild, A. A. High, Y. Zhou, G. Scuri, K. De Greve, A. Sushko, C.-H. Yu, T. Taniguchi, K. Watanabe, D. J. Needleman, M. D. Lukin, H. Park, and P. Kim, Electrical control of interlayer exciton dynamics in atomically thin heterostructures, *Science* **366**, 870 (2019).
- [15] P. Rivera, J. R. Schaibley, A. M. Jones, J. S. Ross, S. Wu, G. Aivazian, P. Klement, K. Seyler, G. Clark, N. J. Ghimire, J. Yan, D. G. Mandrus, W. Yao, and X. Xu, Observation of

- long-lived interlayer excitons in monolayer MoSe₂–WSe₂ heterostructures, *Nat. Commun.* **6**, 6242 (2015).
- [16] P. Rivera, K. L. Seyler, H. Yu, J. R. Schaibley, J. Yan, D. G. Mandrus, W. Yao, and X. Xu, Valley-Polarized exciton dynamics in a 2D semiconductor heterostructure, *Science* **351**, 688 (2016).
- [17] J. Wang, J. Ardelean, Y. Bai, A. Steinhoff, M. Florian, F. Jahnke, X. Xu, M. Kira, J. Hone, and X.-Y. Zhu, Optical generation of high carrier densities in 2D semiconductor heterobilayers, *Sci. Adv.* **5**, eaax0145 (2019).
- [18] F. Ceballos, M. Z. Bellus, H. Y. Chiu, and H. Zhao, Ultrafast charge separation and indirect exciton formation in a MoS₂–MoSe₂ van der waals heterostructure, *ACS Nano* **8**, 12717 (2014).
- [19] H. Chen, X. Wen, J. Zhang, T. Wu, Y. Gong, X. Zhang, J. Yuan, C. Yi, J. Lou, P. M. Ajayan, W. Zhuang, G. Zhang, and J. Zheng, Ultrafast formation of interlayer hot excitons in atomically thin MoS₂/WS₂ heterostructures, *Nat. Commun.* **7**, 12512 (2016).
- [20] X. Hong, J. Kim, S.-F. Shi, Y. Zhang, C. Jin, Y. Sun, S. Tongay, J. Wu, Y. Zhang, and F. Wang, Ultrafast charge transfer in atomically thin MoS₂/WS₂ heterostructures, *Nat. Nanotechnol.* **9**, 682 (2014).
- [21] J. Kunstmann, F. Mooshammer, P. Nagler, A. Chaves, F. Stein, N. Paradiso, G. Plechinger, C. Strunk, C. Schüller, G. Seifert, D. R. Reichman, and T. Korn, Momentum-Space indirect interlayer excitons in transition-metal dichalcogenide van der waals heterostructures, *Nat. Phys.* **14**, 801 (2018).
- [22] N. R. Wilson, P. V Nguyen, K. Seyler, P. Rivera, A. J. Marsden, Z. P. L. Laker, G. C. Constantinescu, V. Kandyba, A. Barinov, N. D. M. Hine, X. Xu, and D. H. Cobden, Determination of band offsets, hybridization, and exciton binding in 2d semiconductor heterostructures, *Sci. Adv.* **3**, e1601832 (2017).
- [23] F. Wu, T. Lovorn, and A. H. MacDonald, Theory of optical absorption by interlayer excitons in transition metal dichalcogenide heterobilayers, *Phys. Rev. B* **97**, 035306 (2018).
- [24] H. Yu, G. Bin Liu, and W. Yao, Brightened spin-triplet interlayer excitons and optical selection rules in van der waals heterobilayers, *2D Mater.* **5**, 035021 (2018).
- [25] T. Woźniak, P. E. Faria Junior, G. Seifert, A. Chaves, and J. Kunstmann, Exciton g factors of van der waals heterostructures from first-principles calculations, *Phys. Rev. B* **101**, 235408 (2020).
- [26] L. Zhang, R. Gogna, G. W. Burg, J. Horng, E. Paik, Y.-H. Chou, K. Kim, E. Tutuc, and H. Deng, Highly valley-polarized singlet and triplet interlayer excitons in van der waals heterostructure, *Phys. Rev. B* **100**, 041402(R) (2019).
- [27] T. Wang, S. Miao, Z. Li, Y. Meng, Z. Lu, Z. Lian, M. Blei, T. Taniguchi, K. Watanabe, S. Tongay, D. Smirnov, and S.-F. Shi, Giant valley-zeeman splitting from spin-singlet and spin-triplet interlayer excitons in WSe₂/MoSe₂ heterostructure, *Nano Lett.* **20**, 694 (2020).
- [28] A. Delhomme, D. Vaclavkova, A. Slobodeniuk, M. Orlita, M. Potemski, D. M. Basko, K. Watanabe, T. Taniguchi, D. Mauro, C. Barreateau, E. Giannini, A. F. Morpurgo, N. Ubrig, and C. Faugeras, Flipping exciton angular momentum with chiral phonons in MoSe₂/WSe₂ heterobilayers, *2D Mater.* **7**, 041002 (2020).
- [29] H. Yu, G.-B. Liu, J. Tang, X. Xu, and W. Yao, Moiré excitons: from programmable quantum emitter arrays to spin-orbit-coupled artificial lattices, *Sci. Adv.* **3**, e1701696 (2017).
- [30] F. Wu, T. Lovorn, and A. H. MacDonald, Topological Exciton Bands in Moiré Heterojunctions, *Phys. Rev. Lett.* **118**, 147401 (2017).
- [31] C.-K. Shih, L.-J. Li, X. Ren, C. Zhang, C. Jin, M.-Y. Chou, C.-P. Chuu, and M.-Y. Li, Interlayer couplings, moiré patterns, and 2d electronic superlattices in MoS₂/WSe₂ hetero-Bilayers, *Sci. Adv.* **3**, e1601459 (2017).
- [32] C. Jin, E. C. Regan, A. Yan, M. Iqbal Bakti Utama, D. Wang, S. Zhao, Y. Qin, S. Yang, Z. Zheng, S. Shi, K. Watanabe, T. Taniguchi, S. Tongay, A. Zettl, and F. Wang, Observation of moiré excitons in WSe₂/WS₂ heterostructure superlattices, *Nature (London)* **567**, 76 (2019).
- [33] N. Zhang, A. Surrente, M. Baranowski, D. K. Maude, P. Gant, A. Castellanos-Gomez, and P. Plochocka, Moiré intralayer excitons in a MoSe₂/MoS₂ heterostructure, *Nano Lett.* **18**, 7651 (2018).
- [34] Y. Tang, L. Li, T. Li, Y. Xu, S. Liu, K. Barmak, K. Watanabe, T. Taniguchi, A. H. MacDonald, J. Shan, and K. F. Mak, Simulation of hubbard model physics in WSe₂/WS₂ moiré superlattices, *Nature (London)* **579**, 353 (2020).
- [35] G. Scuri, T. I. Andersen, Y. Zhou, D. S. Wild, J. Sung, R. J. Gelly, D. Bérubé, H. Heo, L. Shao, A. Y. Joe, A. M. Mier Valdivia, T. Taniguchi, K. Watanabe, M. Lončar, P. Kim, M. D. Lukin, and H. Park, Electrically Tunable Valley Dynamics in Twisted WSe₂/WSe₂ Bilayers, *Phys. Rev. Lett.* **124**, 217403 (2020).
- [36] T. I. Andersen, G. Scuri, A. Sushko, K. De Greve, J. Sung, Y. Zhou, D. S. Wild, R. J. Gelly, H. Heo, D. Bérubé, A. Y. Joe, L. A. Jauregui, K. Watanabe, T. Taniguchi, P. Kim, H. Park, and M. D. Lukin, Excitons in a reconstructed moiré potential in twisted WSe₂/WSe₂ homobilayers, *Nat. Mater.* **20**, 480 (2021).
- [37] K. L. Seyler, P. Rivera, H. Yu, N. P. Wilson, E. L. Ray, D. Mandrus, J. Yan, W. Yao, and X. Xu, Signatures of moiré-trapped valley excitons in MoSe₂/WSe₂ heterobilayers, *Nature (London)* **567**, 66 (2018).
- [38] K. Tran, G. Moody, F. Wu, X. Lu, J. Choi, K. Kim, A. Rai, D. A. Sanchez, J. Quan, A. Singh, J. Embley, A. Zepeda, M. Campbell, T. Autry, T. Taniguchi, K. Watanabe, N. Lu, S. K. Banerjee, K. L. Silverman, S. Kim *et al.*, Evidence for moiré excitons in van der waals heterostructures, *Nature (London)* **567**, 71 (2019).
- [39] H. Baek, M. Brotons-Gisbert, Z. X. Koong, A. Campbell, M. Rambach, K. Watanabe, T. Taniguchi, and B. D. Gerardot, Highly energy-tunable quantum light from moiré-trapped excitons, *Sci. Adv.* **6**, eaba8526 (2020).
- [40] Y. Bai, L. Zhou, J. Wang, W. Wu, L. J. McGilly, D. Halbertal, C. F. B. Lo, F. Liu, J. Ardelean, P. Rivera, N. R. Finney, X. C. Yang, D. N. Basov, W. Yao, X. Xu, J. Hone, A. N. Pasupathy, and X. Y. Zhu, Excitons in strain-induced one-dimensional moiré potentials at transition metal dichalcogenide heterojunctions, *Nat. Mater.* **19**, 1068 (2020).
- [41] M. Brotons-Gisbert, H. Baek, A. Molina-Sánchez, A. Campbell, E. Scerri, D. White, K. Watanabe, T. Taniguchi, C. Bonato, and B. D. Gerardot, Spin–Layer locking of interlayer excitons trapped in moiré potentials, *Nat. Mater.* **19**, 630 (2020).
- [42] See Supplemental Material at <http://link.aps.org/supplemental/10.1103/PhysRevB.103.L161411> for additional details regard-

- ing experimental methods, theoretical discussions of the electrostatics, interlayer exciton selection rules and expected g-factors, supporting magnetic field data, analysis of the charged interlayer exciton lifetimes, further discussions on the transport and electroluminescence measurements, and it includes Refs. [9–11,14,23–25,29,37,44,46–54].
- [43] Y. Zhou, G. Scuri, D. S. Wild, A. A. High, A. Dibos, L. A. Jauregui, C. Shu, K. de Greve, K. Pistunova, A. Y. Joe, T. Taniguchi, K. Watanabe, P. Kim, M. D. Lukin, and H. Park, Probing dark excitons in atomically thin semiconductors via near-field coupling to surface plasmon polaritons, *Nat. Nanotechnol.* **12**, 856 (2017).
- [44] X.-X. Zhang, Y. You, S. Y. F. Zhao, and T. F. Heinz, Experimental Evidence for Dark Excitons in Monolayer WSe₂, *Phys. Rev. Lett.* **115**, 257403 (2015).
- [45] J. P. Echeverry, B. Urbaszek, T. Amand, X. Marie, and I. C. Gerber, Splitting between bright and dark excitons in transition metal dichalcogenide monolayers, *Phys. Rev. B* **93**, 121107(R) (2016).
- [46] G. Wang, L. Bouet, M. M. Glazov, T. Amand, E. L. Ivchenko, E. Palleau, X. Marie, and B. Urbaszek, Magneto-optics in transition metal diselenide monolayers, *2D Mater.* **2**, 034002 (2015).
- [47] D. V. Rybkovskiy, I. C. Gerber, and M. V. Durnev, Atomically inspired k-p approach and valley zeeman effect in transition metal dichalcogenide monolayers, *Phys. Rev. B* **95**, 155406 (2017).
- [48] K. F. Mak, K. He, C. Lee, G. H. Lee, J. Hone, T. F. Heinz, and J. Shan, Tightly bound trions in monolayer MoS₂, *Nat. Mater.* **12**, 207 (2012).
- [49] P. Back, M. Sidler, O. Cotlet, A. Srivastava, N. Takemura, M. Kroner, and A. Imamoğlu, Giant Paramagnetism-Induced Valley Polarization of Electrons in Charge-Tunable Monolayer MoSe₂, *Phys. Rev. Lett.* **118**, 237404 (2017).
- [50] S. Larentis, H. C. P. Movva, B. Fallahzad, K. Kim, A. Behroozi, T. Taniguchi, K. Watanabe, S. K. Banerjee, and E. Tutuc, Large effective mass and interaction-enhanced zeeman splitting of k-valley electrons in MoSe₂, *Phys. Rev. B* **97**, 201407(R) (2018).
- [51] A. Kormányos, G. Burkard, M. Gmitra, J. Fabian, V. Zólyomi, N. D. Drummond, and V. Fal'ko, k-p theory for two-dimensional transition metal dichalcogenide semiconductors, *2D Mater.* **2**, 022001 (2015).
- [52] C. Robert, D. Lagarde, F. Cadiz, G. Wang, B. Lassagne, T. Amand, A. Balocchi, P. Renucci, S. Tongay, B. Urbaszek, and X. Marie, Exciton radiative lifetime in transition metal dichalcogenide monolayers, *Phys. Rev. B* **93**, 205423 (2016).
- [53] M. Palummo, M. Bernardi, and J. C. Grossman, Exciton radiative lifetimes in two-dimensional transition metal dichalcogenides, *Nano Lett.* **15**, 2794 (2015).
- [54] Z. Wang, D. A. Rhodes, K. Watanabe, T. Taniguchi, J. C. Hone, J. Shan, and K. F. Mak, Evidence of high-temperature exciton condensation in two-dimensional atomic double layers, *Nature (London)* **574**, 76 (2019).
- [55] K. Wang, K. De Greve, L. A. Jauregui, A. Sushko, A. High, Y. Zhou, G. Scuri, T. Taniguchi, K. Watanabe, M. D. Lukin, H. Park, and P. Kim, Electrical control of charged carriers and excitons in atomically thin materials, *Nat. Nanotechnol.* **13**, 128 (2018).